





Anomalous temperature dependence of multiple Andreev reflections in a topological insulator Josephson junction

Tobias W Schmitt^{1,2} , Benedikt Frohn¹, Wilhelm Wittl¹, Abdur R Jalil¹, Michael Schleenvoigt¹, Erik Zimmermann¹ , Anne Schmidt¹, Thomas Schäpers¹ , Juan Carlos Cuevas³, Alexander Brinkman⁴, Detlev Grützmacher^{1,2} and Peter Schüffegen^{1,*} 

¹ Peter Grünberg Institute 9, Forschungszentrum Jülich & JARA Jülich-Aachen Research Alliance, Jülich, Germany

² JARA-Institute for Green IT, RWTH Aachen University, Aachen, Germany

³ Departamento de Física Teórica de la Materia Condensada and Condensed Matter Physics Center (IFIMAC), Universidad Autónoma de Madrid, Madrid, Spain

⁴ MESA+ Institute for Nanotechnology, University of Twente, Enschede, The Netherlands

E-mail: p.schueffegen@fz-juelich.de

Received 20 May 2022, revised 8 November 2022

Accepted for publication 22 November 2022

Published 21 December 2022



Abstract

As a promising platform for unconventional superconductivity, Josephson junctions (JJs) of tetradymite topological insulators (TIs) and s-wave superconductors have been investigated in recent years. This family of TI materials, however, often suffers from spurious bulk transport, which hampers the observation of the exotic physics of their topological surface states. Thus, disentangling the transport mechanism of bulk and surface contributions in TI JJs is of high importance when investigating proximity induced superconductivity in those crystals. In this work, we add to the insights regarding these contributions by studying the temperature-dependent behaviour of a Bi₂Te₃-based JJ with transparent interfaces. In electrical transport measurements, we investigate differential conductance spectra of multiple Andreev reflections (MARs) and find a qualitative temperature-dependent change from peak features at low temperatures to dip features at higher ones. The observation of both kind of MAR patterns in a single JJ suggests contributions of diffusive bulk and ballistic surface states and links to a similar finding in the temperature dependence of the critical current. Our work advances the research of induced superconductivity in TIs and offers new avenues to study the induced superconductivity in the topological surface states of these materials.

Keywords: topological insulators, Josephson junctions, multiple Andreev reflection

(Some figures may appear in colour only in the online journal)

* Author to whom any correspondence should be addressed.



Original content from this work may be used under the terms of the [Creative Commons Attribution 4.0 licence](https://creativecommons.org/licenses/by/4.0/). Any further distribution of this work must maintain attribution to the author(s) and the title of the work, journal citation and DOI.

1. Introduction

The prediction of unconventional superconductivity in the proximitized surface of topological insulators (TIs) [1] triggered many experimental efforts to investigate TI-superconductor (S) hybrid devices. Among the first TIs was the family of tetradymite compounds like Bi_2Te_3 , Sb_2Te_3 or Bi_2Se_3 , which offer a large bulk band gap for accessing the topological surface states [2]. Pioneering work investigating Josephson junctions (JJs) on exfoliated flakes demonstrated a superconducting proximity effect in these materials [3, 4] and has subsequently been extended to epitaxially grown binary, ternary and quaternary TIs. However, a major obstacle for the investigation of the induced superconductivity in the topological surface states of these materials is the presence of undesired bulk channels, particularly for the binary compounds. While bulk conduction often dominates signatures in normal transport characterization and impedes the visibility of the surface states, a recent work on $(\text{Bi,Sb})_2\text{Te}_3$ -based JJs managed to distinguish bulk and surface contributions to a supercurrent by the distinct temperature dependence in these different transport regimes [5].

In addition to the characterization of the superconducting state, it is worthwhile to study S-TI-S JJs also in the dissipative state where the differential conductance can show a subharmonic gap structure (SGS) [6–10]. The SGS features are typically attributed to resonances from multiple Andreev reflections (MARs) and expected to appear at voltages of $V = 2\Delta/en$ with Δ being the superconducting gap, e the elementary charge and n an integer [11, 12]. The exact shape of the SGS, e.g. if the features appear as differential conductance dips or peaks, depends on the transport characteristics in the junction and can hence reveal valuable insights [13, 14]. In this spirit, MAR signatures have for example already been used to estimate the transparency of ballistic channels in JJs [15] and they have been theoretically predicted as an indicator for a topological transition in semiconductor nanowires [16]. As the SGS also differs significantly for JJs in the diffusive limit compared to ballistic ones [13, 14], we investigate in this work the SGS of a TI JJ for distinct MAR contributions of diffusive bulk and ballistic surface states.

2. Methods

2.1. Fabrication

For the fabrication of TI JJs we use an ultra-high vacuum (UHV) process based on a monolithically integrated stencil mask [5]. This process combines the selective area growth of TI materials via molecular beam epitaxy (MBE) and the deposition and patterning of superconducting electrodes under UHV conditions. It thus allows to create a pristine interface between the deposited S and the TI material. Furthermore, it allows to conserve the TI weak link *in situ* with an amorphous Al_2O_3 capping and thereby prevents degradation of the TI's surface. As a TI material for our study in this work we choose Bi_2Te_3 which is typically n-type doped and shows a

large bulk conduction in normal transport characterization (see appendix A). As parent S we use Al with a small adhesion layer of 3 nm Nb for interface engineering (see appendix B).

We start the fabrication with a Si(111) substrate with a resistivity $>2000 \Omega \text{ cm}$. The SiO_2 and Si_3N_4 layers for the stencil mask are deposited via low pressure chemical vapour deposition (LPCVD). The mask layout is structured in the top Si_3N_4 layer via electron beam lithography and reactive ion etching. Subsequently, the sample surface is cleaned with Piranha solution ($\text{H}_2\text{O}_2 + \text{H}_2\text{SO}_4$ (1:2)) and the sacrificial layer of SiO_2 is etched wet chemically using hydrofluoric acid (HF 1%). The sample is then loaded into the MBE chamber and heated to 700°C prior to selective area growth of a 15 nm Bi_2Te_3 thin film under continuous sample rotation. For the deposition of metals, the sample is cooled below 0°C and layers of 3 nm Nb and 40 nm Al are deposited without sample rotation using an electron beam evaporator. Finally, a 5 nm Al_2O_3 capping layer is applied under rotation to protect the TI from degradation at ambient conditions. The sample is then taken out of the MBE chamber and most of the excessive Nb/Al stack on the stencil mask (except in the very proximity of the JJ) is etched using standard photolithography techniques and wet chemical etching. This yields pairs of well-defined bond pads which are interconnected by an *in situ* fabricated JJ.

In figure 1(a), a top view false-color scanning electron micrograph of the fabricated JJ is shown. In a bright contrast, the free-standing stencil mask can be seen (with the metallic layer on the mask not colored for clarity). The small separation between the Nb/Al electrodes on the Bi_2Te_3 film originates from the shadow of the stencil mask during the deposition and represents the JJ with a length of $L = 80 \text{ nm}$ and a width of $W = 1 \mu\text{m}$. A cross-sectional schematic of the lateral junction geometry is depicted in figure 1(b). An effective superconducting gap $\Delta^* < \Delta_S$ is expected to be induced in the Bi_2Te_3 under the electrodes whose magnitude depends on the interface transparency parameter γ_B (with $\gamma_B = 0$ for a perfectly transparent interface and $\gamma_B \rightarrow \infty$ for a vanishingly small interface transparency) [17]. The interface of the TI under the electrodes (light green in figure 1(b)) to the uncovered TI in the junction (dark green in figure 1(b)) can be seen as effective interface for Andreev reflections, which might add an additional barrier, e.g. due to a Fermi velocity mismatch.

The characteristics of this JJ depend on the transport properties of the Bi_2Te_3 weak link. The MBE-grown Bi_2Te_3 thin films are typically unintentionally n-type doped and show diffusive bulk transport (blue) superimposed by transport mediated via topologically protected surface states (red). In normal transport measurements the bulk transport usually dominates and has been characterized by magneto-transport measurements (see appendix A or [18, 19]). While the phase coherence length l_φ is usually found to be several hundreds of nm, the electron mean free path $l_{e, \text{bulk}}$ ranges typically only around a few nm. This also links to a short superconducting coherence length of the bulk states $\xi_{\text{bulk}} = \xi_{\text{diff}} = \sqrt{\frac{\hbar D}{\Delta^*}}$ with $D = \frac{1}{3} l_{e, \text{bulk}} v_F$ being the diffusion constant. Assuming a Fermi

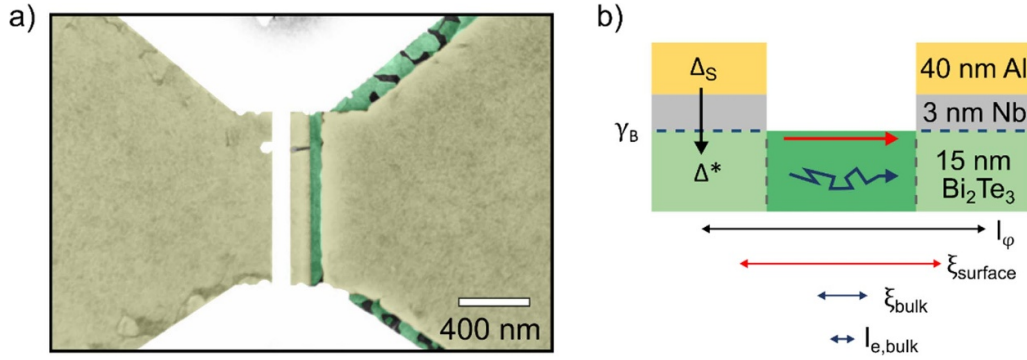


Figure 1. Topological insulator Josephson junction with Al electrodes. (a) Top-view on a false-colored scanning electron micrograph of a Josephson junction fabricated via stencil lithography. The Bi_2Te_3 thin film (green) is grown selectively on the Si surface (black) and contacted by the two Al/Nb electrodes (yellow). The free-standing mask has a bright contrast and metals on top of the mask are not colored for clarity. (b) Cross-sectional schematic of a topological insulator Josephson junction. The transport in the junction is governed by both bulk (blue) and surface (red) states. The important length scales for the classification of the junction are illustrated below the schematic.

velocity of $v_F = 4.3 \cdot 10^5 \frac{\text{m}}{\text{s}}$ (determined by angle-resolved photoemission spectroscopy on Bi_2Te_3 thin films [20]), an electron mean free path of $l_{e, \text{bulk}} \approx 1 - 10 \text{ nm}$ and an induced gap of $\Delta^* \approx 160 \mu\text{eV}$ yields $\xi_{\text{bulk}} \approx 20 - 80 \text{ nm}$. Hence, for the bulk channels the JJ is expected to be in the phase-coherent, diffusive regime with intermediate length. For the surface states, on the other hand, the electron mean free path $l_{e, \text{surface}}$ can often not be determined straight-forwardly from normal transport measurements due to the large bulk contributions. However, from observations of Shubnikov-de Haas oscillations [18] it can be estimated to be longer than the bulk electron mean free path and we assume the junction to be in a (quasi-) ballistic regime ($l_{e, \text{surface}} \sim L$) for the surface states. In this case, the superconducting coherence length ξ_{surface} is expected to range between ξ_{diff} ($l_{e, \text{surface}} = L$) $\approx 260 \text{ nm}$ and $\xi_{\text{ball}} = \frac{\hbar v_F}{\Delta^*} \approx 1.77 \mu\text{m}$ implying that for the surface channels the junction is expected to be in the short junction limit.

3. Results

We characterized our as-fabricated JJ with current biased quasi four-point electrical transport measurements in a dilution refrigerator equipped with commercially available RF + RC filters [21] and a base temperature of $T < 50 \text{ mK}$. The IV curve of the junction is displayed in figure 2 for different sweeping directions of the bias current. At high bias currents the IV curve is linear and we extract a normal resistance of $R_n = 58 \Omega$ from a fit to this region (black dashed lines in figure 2). When the voltage over the junction is below $2\Delta^*/e$ (indicated by red dotted line), we observe a deviation from this linear behaviour in the IV characteristics. This is a common signature of an excess current carried by Andreev reflections in the junction, which we determine to $I_{\text{exc}} = 2.37 \mu\text{A}$. It should be noted that we observe additional features in differential measurements at even higher bias currents that, however, scale in temperature with a smaller superconducting gap and disappear above a temperature of $T = 1.1 \text{ K}$ (see appendix C, figure S2). At low bias currents, we observe a supercurrent of $I_c = 2.22 \mu\text{A}$ and a retrapping current of $I_r = 0.89 \mu\text{A}$ (see inset figure 2).

A similar hysteretic behaviour is often reported in measurements of coplanar JJs and origins from heating effects in the resistive state of the junction [22]. The magnitude of both critical current and excess current can be related to the superconducting gap and these values are often taken as a preliminary reference for the quality of the junction. However, their theoretical values also depend on the limit of the junction. In the short junction limit $\xi_{\text{diff/ball}} \gg L$, for instance, the excess current in a fully transparent, ballistic junction is described by $eI_{\text{exc}}R_n/\Delta^* = 8/3 \approx 2.67$ [23] while it has been found to be $eI_{\text{exc}}R_n/\Delta^* = (\pi^2/4 - 1) \approx 1.47$ [24, 25] for diffusive channels. In longer diffusive junctions ($\xi_{\text{diff}} \sim L$ or $\xi_{\text{diff}} \ll L$), both the excess current and the critical current have been found to decrease with an increasing ratio L/ξ_{diff} [14, 26]. For our junction we find $eI_{\text{exc}}R_n/\Delta^* \approx 0.86$ and $eI_cR_n/\Delta^* \approx 0.8$. By assuming only diffusive bulk transport this fits to an intermediate long junction regime ($L/\xi_{\text{diff}} \approx 2 - 3$) [14]. Possible additional contributions from the (quasi-) ballistic surface states in eI_cR_n/Δ^* and $eI_{\text{exc}}R_n/\Delta^*$, however, would decrease the relative bulk contribution and accordingly indicate a higher L/ξ_{diff} ratio for the bulk channels.

In order to study the SGS of the TI JJ, we further investigated the sample with differential measurements using standard lock-in techniques. While in the dissipative regime of interest the constant voltage over the junction causes an ac Josephson effect and thus ac currents, our measurements only probe the dc current component and the respective differential conductance. In figure 3(a), the differential conductance spectrum at low temperatures ($T = 0.1 \text{ K}$) is shown to reveal a rich SGS within the gap region ($|V| < 2\Delta^*/e$). As mentioned above, the MAR features depend on the characteristics of the junction and they are often observed as differential conductance peaks or dips at voltages $|V| = 2\Delta^*/en$ with n being an integer in short JJs ($L \ll \xi$). For diffusive channels in an intermediate long phase-coherent regime ($\xi_{\text{diff}} < L < l_\varphi$), the conductance features of MARs have been calculated by Cuevas *et al* [14] (under the assumption of fully transparent SN interfaces). Our low temperature differential conductance data (figure 3(a)) fit well to their simulation for $L = 4\xi_{\text{diff}}$ shown in figure 3(b) and we extract an induced gap of $\Delta^* = 158 \mu\text{eV}$ from the

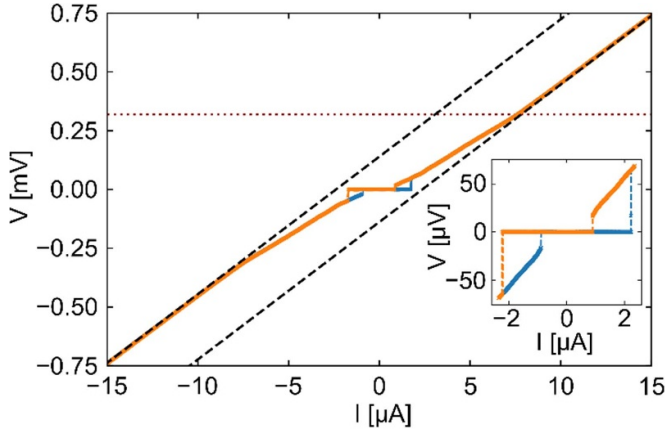


Figure 2. IV characteristics of the junction. The up sweep is shown in blue and the down sweep in orange. The black dashed lines are linear fits to the region at high bias currents. For positive voltages, the red dotted line marks the value $2\Delta^*/e$. Inset shows three up and three down sweeps with a fine stepping and I_C/I_T are extracted from the mean value.

differential conductance feature positions in the measurement. Both the observation of MARs as well as the large magnitude of the induced gap (with respect to the critical temperature, see below) are indications for transparent interfaces. We continued the SGS measurements at higher temperatures and found that the differential conductance spectrum looks quite different in this temperature regime (figure 3(c)). While a scaling of the feature position with the decrease of the induced gap at higher temperatures is expected and has been reported in many experiments, we observe an overall change in the pattern. Most interestingly, we find dips instead of peaks at the voltages $|V| = 2\Delta^*/en$. Similar differential conductance dip features have, for example, recently been observed in Bi_2Se_3 [7] or InAs 2DEG [15] JJs and their appearance has been linked to highly transparent ballistic channels. A simulated curve based on [13] for such a high interface transparency is shown in figure 3(d).

We further study this transition in the full temperature dependence of the MAR features shown in figure 4(a). The low/high temperature conductance spectra from figure 3 can be observed over a range of temperatures with a crossover starting below $T = 1$ K. While the change first seems to affect mainly the spectrum at lower energies a gradual transition can be observed at the higher energy features (with the measurements at temperatures of $T \approx 0.8$ K showing features of both spectra, see black arrows in figures 4(a) and (c)). In order to study the temperature dependence of the induced gap, we extract the position of the three highest MAR features at both low and high temperatures. The curves within the transition are skipped as the feature position cannot be assigned unambiguously. The extracted peak positions are shown in figure 4(b). For the analysis we plot the temperature dependence of an induced gap next to the data [17]:

$$\Delta^*(T) = \frac{\Delta_{\text{BCS}}(T)}{1 + \gamma_B \sqrt{\Delta_{\text{BCS}}(T)^2 - \Delta^*(T)^2} / \pi k_B T_c} \quad (1)$$

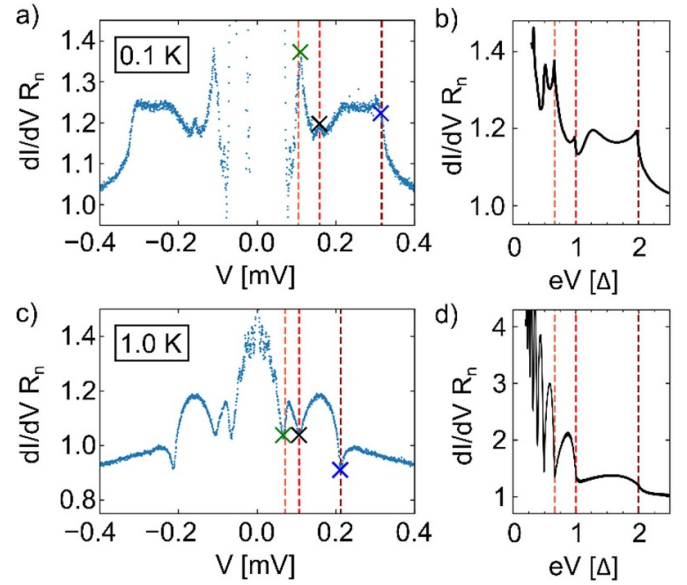


Figure 3. Conductance spectra and simulations of multiple Andreev reflections. (a) Measured conductance spectrum at $T = 0.1$ K. (b) Simulated conductance spectrum for a diffusive SNS junction with $L = 4\xi$. Reprinted figure with permission from [14], Copyright (2006) by the American Physical Society. (c) Measured conductance spectrum at $T = 1$ K. (d) Simulated conductance spectrum for a single-mode, short SNS junction with a transparency $D = 0.9$ (no other scattering in the vicinity of the junction) following [13]. The dashed lines in all curves correspond to $2\Delta^*$ (dark red), Δ^* (red) and $2\Delta^*/3$ (light red) with $\Delta^*(0.1 \text{ K}) = 158 \mu\text{eV}$ and $\Delta^*(1 \text{ K}) = 106 \mu\text{eV}$. The crosses mark the features in the measurement data (analogue to figure 4(a)).

Where $\Delta_{\text{BCS}}(T)$ describes the temperature dependence of the gap of a Bardeen-Cooper-Schrieffer (BCS) S with a critical temperature T_c . We find the best match for the Δ^* feature of the low-temperature data using $\gamma_B = 0.45$ and $T_c = 1.15$ K (using an interpolation formula [27] for the BCS gap). For the $2\Delta^*$ and $2\Delta^*/3$ traces the curve has been scaled respectively, yielding the red curves figure 4(b). In addition to the induced gap temperature dependence, figure 4(b) shows the pure BCS gap $\Delta_{\text{BCS}}(T)$ (solid grey lines) and a rescaled version of this BCS gap scaled to the low-temperature limit of the induced gap (dashed grey lines). While it is arguable that the induced gap dependence fits better to the data than a (re-scaled) BCS gap, it should be emphasized that this needs to be taken with caution as we could not extract values in the intermediate temperature regime where the difference would be most clear and we rely on the extraction of both type of MAR features. We use the extracted data of the temperature-dependent gap $\Delta^*(T)$ to show the anomalous temperature-dependent change in the three highest MAR features by scaling the dc voltage of spectra at five different temperatures to the respective induced gap (figure 4(c)). The characteristic change of the MAR pattern for these features can be compared to simulations of MAR patterns for a purely diffusive junction shown in figure 4(d). Unlike the measurements, these simulations only predict a gradual decrease of the feature size with increasing temperature and no other distinct change in their appearance.

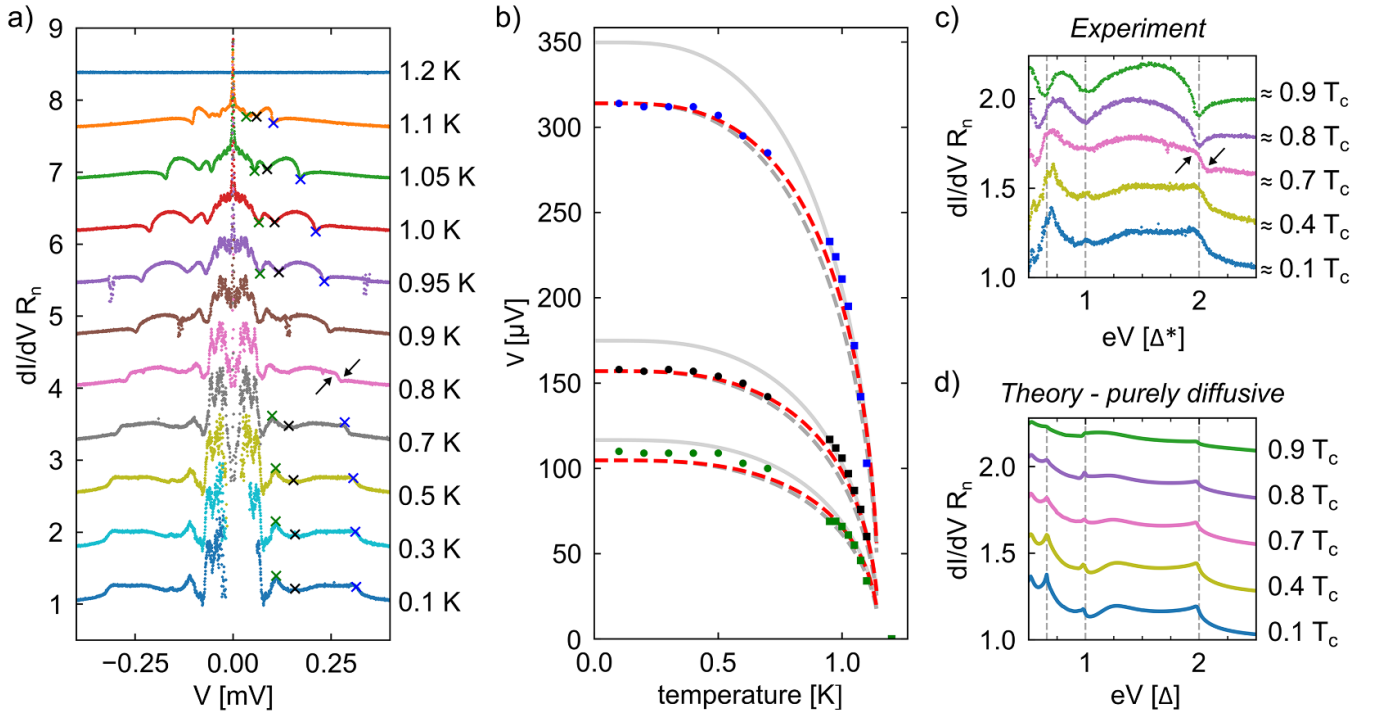


Figure 4. Temperature dependence of MAR spectra. (a) MAR spectra at different temperatures from $T = 1.2$ K down to $T = 0.1$ K (with more curves shown for the faster change at higher temperatures). The positions of the MAR features have been marked with crosses on the positive branch for $2\Delta^*$ (blue), Δ^* (black) and $2\Delta^*/3$ (green). At intermediate temperatures both dip and peak features are present (black arrows at 0.8 K curve) so that the feature position could not be assigned unambiguously. For visibility the curves are offset by $0.75R_n$. (b) Temperature dependence of MAR feature positions assigned to $2\Delta^*$ (blue), Δ^* (black), and $2\Delta^*/3$ (green). While the boxes indicate the position extracted from dip-like features at higher temperatures, the spheres represent the position extracted from peak-like features at low temperatures. The dashed red lines are plots of equation (1) using $T_c = 1.15$ K and $\gamma_B = 0.45$ and the (dashed) grey lines show the (re-scaled) BCS gap (all three scaled to $2\Delta^*$, Δ^* , and $2\Delta^*/3$). (c) MAR spectra at different temperatures scaled to the temperature-dependent gap Δ^* extracted from feature positions. For the curve at $T = 0.8$ K ($\approx 0.7 T_c$) the interpolation value from the red curve in (b) was used. Grey dashed lines indicate positions of $2\Delta^*$, Δ^* , and $2\Delta^*/3$ respectively. (d) Simulated temperature-dependent MAR spectra for a diffusive SNS junction with $L = 4\xi$ following [14].

4. Discussion

Such a temperature-dependent dip-to-peak transition of MAR features in a single JJ has, to our knowledge, not been observed yet. The IV characteristic and the MAR pattern at low temperatures fit well to the theoretical predictions for the junction regime estimated by normal transport characterization for the diffusive bulk channels. This hence suggests that the transport in the JJ is mainly carried by these bulk states at low temperatures. On the other hand, the MAR features at higher temperatures are not expected to appear for diffusive channels and suggest the presence of ballistic modes mediated by the topological surface states. This observation adds to a previous study of Nb-(Bi,Sb)₂Te₃-Nb JJs, which reported a distinct temperature behaviour of two different contributions to the supercurrent carried by diffusive bulk and ballistic topological surface states [5]. While both contributions are present at low temperatures, the ballistic surface states dominate the supercurrent at higher temperatures. In appendix D, the same analysis for the temperature-dependent critical current of the junction in the present work is shown to yield qualitatively similar results. The qualitative similarity to the temperature dependence of the MAR spectra supports the rationale that the anomalous temperature dependence of MAR spectra originates from distinct contributions of ballistic surface and diffusive bulk channels.

Future studies in different junction regimes will help to study this temperature-dependent transition and its origin in more detail.

5. Conclusion

In this work, we present the study of MAR features in a Bi₂Te₃ based JJ with transparent interfaces. While the transport at low temperatures seems to be mainly governed by diffusive bulk channels we observe an anomalous temperature-dependent dip-to-peak transition in the features of differential conductance spectra. Similar to findings in the temperature dependence of the critical current, we relate the observation of both patterns in different temperature regimes of the same JJ to the presence of ballistic surface states next to the diffusive bulk contributions. Our work hence offers new insights into the distinct contributions in TI JJs and indicates the relevance of the temperature regime when studying their MAR signatures.

Data availability statement

The data that support the findings of this study are available upon reasonable request from the authors.

Acknowledgments

We thank A Hertel for helpful discussions on MARs. Also, we gratefully acknowledge D Rosenbach and A A Golubov for providing codes for the Ic-T fitting. We further thank N Tas and J W Berenschot for the LPCVD deposition of the SiO₂ and Si₃N₄ mask layers. Except for the LPCVD depositions, all fabrication processes were performed at the Helmholtz Nano Facility (HNF) [42]. This work has been supported financially by the German Federal Ministry of Education and Research (BMBF) via the Quantum Future project ‘MajoranaChips’ (Grant No. 13N15264) within the funding program Photonic Research Germany, by Germany’s Excellence Strategy Cluster of Excellence ‘Matter and Light for Quantum Computing’ (ML4Q) EXC 2004/1–390534769 as well as by the Bavarian Ministry of Economic Affairs, Regional Development and Energy within Bavaria’s High-Tech Agenda Project “Bausteine für das Quantencomputing auf Basis topologischer Materialien mit experimentellen und theoretischen Ansätzen” (Grant allocation No. 07 02/686 58/1/21 1/22 2/23). J C C acknowledges funding from the Spanish Ministry of Science and Innovation (Grant No. PID2020-114880GB-I00).

Funding

Deutsche Forschungsgemeinschaft; Ministerio de Ciencia e Innovación; Bayerisches Staatsministerium für Wirtschaft, Landesentwicklung und Energie; Bundesministerium für Bildung und Forschung.

Appendix A. Normal transport characterization

For the characterization of electronic transport in the Bi₂Te₃, we prepared a Hall bar device with a thin film of 15 nm Bi₂Te₃ grown with the same parameters as the JJ sample in a different growth run. The Hall bar substrates, however, did not have a mask for selective area growth/stencil lithography. After MBE growth, the TI thin films were capped with 5 nm Al₂O₃ and 10 μm wide Hall bar devices were patterned using a standard lithography process and reactive ion etching. In a second lithography step, ohmic contacts were deposited by first etching the Al₂O₃ capping layer in the contact area with a TMAH-based developer and subsequent deposition of 50 nm Ti/100 nm Pt electrodes.

An optical micrograph of the bonded Hall bar device is displayed in figure S1(a). On this sample, Hall effect measurements were taken in a cryostat with a base temperature of 1.2 K and magnetic fields up to 14 T. Using standard lock-in measurement techniques, both longitudinal resistivity ρ_{xx} and Hall resistivity ρ_{xy} have been measured as a function of the out-of-plane magnetic field (figure S1(b)). The negative slope of the measured Hall voltage indicates n-type transport typical for MBE grown Bi₂Te₃ films. From the Hall resistance curve, the sheet carrier density is determined to $n_{2D} = 2.55 \times 10^{14} \text{ cm}^{-2}$ and a mobility of $\mu = 121 \frac{\text{cm}^2}{\text{Vs}}$ is extracted. From this, we estimate the 3D charge carrier density to $n_{3D} = n_{2D}/15 \text{ nm} = 1.7 \times 10^{20} \text{ cm}^{-3}$. These values

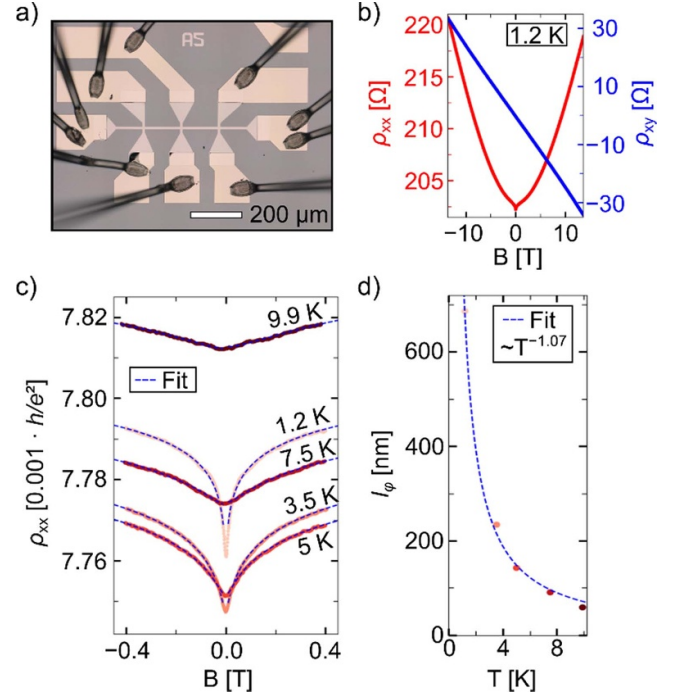


Figure S1. Normal transport characterization of Bi₂Te₃ thin films. (a) Optical micrograph of the Hall bar device. (b) Magnetic field dependence of longitudinal resistivity ρ_{xx} (red) and Hall resistivity ρ_{xy} (blue) at $T = 1.2$ K. (c) Weak anti-localization feature in ρ_{xx} measured at different temperatures. The dashed blue lines are two corresponding fits with the HLN model to the positive and negative magnetic field data. (d) Temperature dependence of the extracted phase coherence length l_ϕ . The values are averaged from both HLN fits of the respective temperature in (c) which, however, show only a small deviation.

are close to the range of previous reports on MBE grown Bi₂Te₃ thin films [19, 28]. The rather high charge carrier density indicates that the Fermi level lays far above the Dirac point in the conduction band and normal transport is dominated by bulk contributions. With the approximation of an open cylindrical Fermi surface at elevated charge carrier densities [29], the in-plane Fermi wave vector can be assumed to $k_{F,xy} = \sqrt{2\pi (n_{3D} \cdot c/\pi)}$ with $c = 3.05$ nm being the out-of-plane lattice parameter of Bi₂Te₃. This Fermi wavevector can be used to estimate the elastic electron mean free path for the bulk to $l_{e,bulk} = \hbar k_{F,xy} \mu / e \approx 8$ nm. This length is on the order of magnitude of previously reported values [19], where a similar calculation yields $l_{e,bulk} \approx 2$ nm. The phase-coherence length is found by fitting with the Hikami–Larkin–Nagaoka (HLN) model [30] to the weak anti-localization feature of the Hall signal. We extract a phase coherence length of $l_\phi \approx 700$ nm at $T = 1.2$ K with a prefactor α close to -0.5 , indicating transport via a single channel.

Appendix B. Properties of the superconductor layer stack

In order to investigate the unconventional superconductivity in more complex topological insulator-superconductor hybrid devices, we aim to use Al as parent superconductor due

its advantageous properties like the reported long timescales for quasiparticles excitations [31], particularly interesting for devices like TI-based superconducting qubits [32] or topological qubit proposals [33]. For the present work, the use of Al also allows to investigate the temperature-dependent transition of the MAR features in a low temperature range $T < 1.3$ K (compared to junctions with Nb ($T_{c,Nb} \approx 9$ K)) and thus reduces thermal noise in the measurements. However, the deposition of pure Al on tetradymite topological insulators has been found to create bad interfaces due to strong interdiffusion [34]. A solution for this problem are interfacial layers to stop the diffusion of Al and allow for a good proximity effect. The impact of such interfacial layers has already been investigated on *ex situ* fabricated Al-Bi₂Te₃-Al and Al-Bi₂Se₃-Al JJs [6, 7, 35]. A natural choice for the investigations of this work forms a thin Nb interfacial layer (see figure 1(b)) which is already known from previous work to form highly transparent interfaces to tetradymite TIs [5]. In the following, we discuss the superconducting properties of this Al/Nb stack and the influence of the thin Nb layer.

At first, we analysed the properties of the 40 nm Al layer by fabricating a reference sample and characterizing the film properties in electrical resistance measurements at low temperatures. We find $T_{c,Al} = 1.3$ K which is close to literature values. In order to determine the impact of the Nb layer under similar conditions as in the JJ experiments, i.e. regarding growth conditions and proximity effects, we prepared a thin film sample with 15 nm Bi₂Te₃ + 3 nm Nb + 40 nm Al (without a stencil mask). For this stack, we find a critical temperature $T_{c,stack} = 2.38$ K. As this critical temperature is higher than $T_{c,Al}$, the thin Nb layer seems to be superconductive itself. Compared to thicker Nb films with $T_{c,Nb} \approx 9$ K, however, the critical temperature of this thin layer is greatly reduced. The superconducting properties of thin Nb films have been studied by Delacour *et al* [36] and a transition at a film thickness of 3 nm has been found. This transition takes place rapidly in a thickness regime of a few Å. For the JJ sample discussed in the main text, the differential conductance measurements directly allow us to determine the critical temperature of the Al/Nb stack at the interface to the TI to be $T_c = 1.15$ K which is smaller than the critical temperature observed for the reference sample. As our reference measurements show that the Nb interlayer is right at the border to the superconducting regime and we do not see such an increased critical temperature in the JJ, we think that the interfacial Nb layer in our JJs is slightly thinner than for the control chip with the Nb being in a metallic state or in a superconductive state with a critical temperature even lower than 2.38 K.

Appendix C. Differential conductance at higher biases

Additional to the temperature-dependent MAR data shown in the main text figure 4(a) we also measured the differential conductance up to higher bias currents (figure S2). Here, additional features are visible outside of the induced superconducting gap whose position might be interpreted as

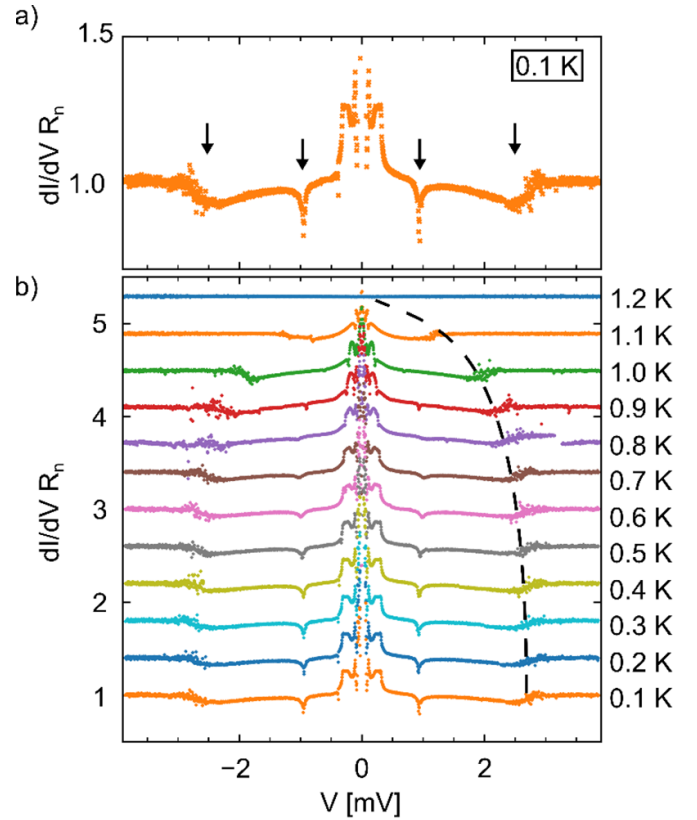


Figure S2. Additional differential conductance features at voltages higher than $2\Delta^*$. (a) Differential conductance measurement up to a dc voltage of $V = \pm 3.9$ mV at a temperature of $T = 0.1$ K. Arrows indicate additional features present at $|V| \gg 2\Delta^*$. (b) Differential conductance at higher biases for various temperatures. Dashed line indicates scaling of the higher bias features similar to the induced superconducting gap shown in figure 4(b). Curves shifted for clarity by $0.4 R_n$.

gap features of Nb ($\Delta \approx 1.3$ meV). The features, however, scale in temperature qualitatively like the (smaller) induced superconducting gap and vanish at $T = 1.2$ K. This speaks against their assignment to a superconducting gap higher than the observed induced gap and it is more likely that they are related to heating effects in the electrodes or the lateral coplanar JJ geometry itself as suggested for similar observations in previous work on SNS JJs [6, 15, 37, 38]. Below a temperature of $T = 0.8$ K, we observe additionally a small change in the differential conductance at high biases (visible in figure S2(b) by a smaller offset between 0.8 K and 0.7 K curve) corresponding to a change in differential resistance of a few Ohm.

Appendix D. Temperature dependence of the critical current

The interpretation of the temperature-dependent MAR data in the main text as signatures of diffusive bulk and ballistic surface states links to a similar observation in the temperature dependence of the critical current by Schüffelgen *et al* [5]. In order to support the link between both signatures, we additionally measured and analysed $I_c(T)$ data of the junction

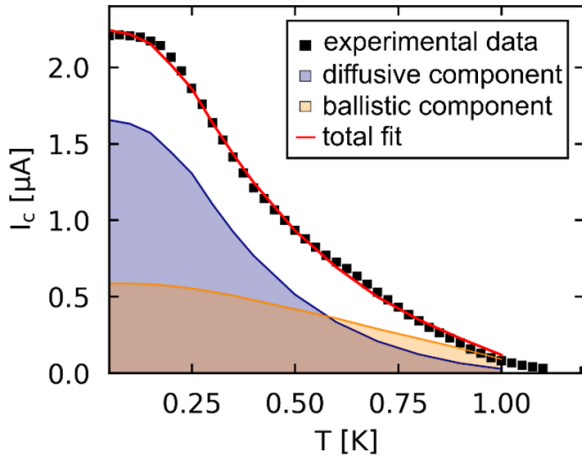


Figure S3. Temperature dependence of the critical current of the Josephson junction. The data have been extracted from IV curves at the respective temperature by using a criterion of $V_{\text{crit}} = 2 \mu\text{V}$. Each black point is averaged from three up and three down sweeps. For the total fit (red) to the data the ballistic (orange) and diffusive (blue) components are added.

in the main text. These data are shown as black points in figure S3. Around a temperature of $T = 0.45 \text{ K}$ there is a ‘kink’ in the slope in the data, suggesting that there are two contributions to the supercurrent with distinct temperature dependence. Next to the data, we show simulations of the temperature dependence of the critical current consisting of two components following [5]. One component is calculated for a short ballistic weak link and the other one for an intermediate long diffusive weak link. The red line in figure S3 shows the combined critical current values of both components.

Analogous to [5] we use the clean limit Eilenberger equations to model the ballistic component of the surface states [39]. As an input parameter we use the critical temperature $T_{\text{c,ball}} = 1.15 \text{ K}$ and the Fermi velocity $v_F = 4.3 \cdot 10^5 \frac{\text{m}}{\text{s}}$. We assume a similar transparency parameter for both interfaces of $D = 0.95$. For the simulation of the diffusive supercurrent component of the bulk, we use the Usadel equations with effective boundary conditions [40, 41]. In accordance with the induced gap scaling extracted from the temperature-dependent MAR data we set the parameter $\gamma_B = 0.5$ and leave the parameter γ , which describes the strength of the proximity effect, as open parameter for the fitting. We use the same critical temperature as for the surface states $T_{\text{c,diff}} = 1.15 \text{ K}$ (as there is no obvious other choice) and vary the parameter $L/\xi_{\text{diff},T_c}$ in the intermediate long regime, with $\xi_{\text{diff},T_c} = \sqrt{\frac{\hbar D}{2\pi k_B T_c}}$ being the coherence length normalized to the critical temperature. For the fitting to our data, we leave the relative scaling of both components free and find a good fit by using the parameters $\gamma = 0.25$ and $\frac{L}{\xi_{\text{diff},T_c}} = 6$. Notice that due to the different normalization of the coherence length ξ_{diff,T_c} compares to the coherence length $\xi_{\text{diff}} = \sqrt{\frac{\hbar D}{\Delta^*}}$ cited in the main text via $\xi_{\text{diff},T_c} \approx 0.5 \xi_{\text{diff}}$.

While we assume in the present case, in contrast to [5], the same critical temperature for both components

($T_{\text{c,ball}} = T_{\text{c,diff}}$), figure S3 clearly shows that their distinct temperature dependence leads to two regimes. At high temperatures, the contribution of the ballistic channels dominate and the diffusive contribution is small. As the temperature is lowered, the diffusive contribution starts to increase faster and is dominant at lower temperatures. While not being directly linked to the SGS, the qualitative similarity of the components to the critical current and the observation of the MAR temperature dependence in the main text is notable.

ORCID iDs

Tobias W Schmitt <https://orcid.org/0000-0001-8531-0742>

Erik Zimmermann <https://orcid.org/0000-0002-1159-2027>

Thomas Schäpers <https://orcid.org/0000-0001-7861-5003>

Peter Schüffegen <https://orcid.org/0000-0001-7977-7848>

References

- [1] Fu L and Kane C L 2008 Superconducting proximity effect and Majorana fermions at the surface of a topological insulator *Phys. Rev. Lett.* **100** 096407
- [2] Zhang H, Liu C-X, Qi X-L, Dai X, Fang Z and Zhang S-C 2009 Topological insulators in Bi_2Se_3 , Bi_2Te_3 and Sb_2Te_3 with a single Dirac cone on the surface *Nat. Phys.* **5** 438–42
- [3] Veldhorst M *et al* 2012 Josephson supercurrent through a topological insulator surface state *Nat. Mater.* **11** 417–21
- [4] Williams J R, Bestwick A J, Gallagher P, Hong S S, Cui Y, Bleich A S, Analytis J G, Fisher I R and Goldhaber-Gordon D 2012 Unconventional Josephson effect in hybrid superconductor-topological insulator devices *Phys. Rev. Lett.* **109** 056803
- [5] Schüffegen P *et al* 2019 Selective area growth and stencil lithography for *in situ* fabricated quantum devices *Nat. Nanotechnol.* **14** 825–31
- [6] Galletti L, Charpentier S, Song Y, Golubev D, Wang S M, Bauch T and Lombardi F 2017 High-transparency $\text{Al}/\text{Bi}_2\text{Te}_3$ double-barrier heterostructures *IEEE Trans. Appl. Supercond.* **27** 1–4
- [7] Kunakova G, Bauch T, Trabaldo E, Andzane J, Erts D and Lombardi F 2019 High transparency Bi_2Se_3 topological insulator nanoribbon Josephson junctions with low resistive noise properties *Appl. Phys. Lett.* **115** 172601
- [8] Jauregui L A, Kayyalha M, Kazakov A, Miotkowski I, Rokhinson L P and Chen Y P 2018 Gate-tunable supercurrent and multiple Andreev reflections in a superconductor-topological insulator nanoribbon-superconductor hybrid device *Appl. Phys. Lett.* **112** 093105
- [9] Kim R-H, Kim N-H, Kim B, Hou Y, Yu D and Doh Y-J 2022 Multiple Andreev reflections in topological insulator nanoribbons *Curr. Appl. Phys.* **34** 107–11
- [10] Ghatak S, Breunig O, Yang F, Wang Z, Taskin A A and Ando Y 2018 Anomalous Fraunhofer patterns in gated Josephson junctions based on the bulk-insulating topological insulator BiSbTeSe_2 *Nano Lett.* **18** 5124–31
- [11] Klapwijk T M, Blonder G E and Tinkham M 1982 Explanation of subharmonic energy gap structure in superconducting contacts *Physica B+C* **109–110** 1657–64
- [12] Octavio M, Tinkham M, Blonder G E and Klapwijk T M 1983 Subharmonic energy-gap structure in superconducting constrictions *Phys. Rev. B* **27** 6739–46

- [13] Averin D and Bardas A 1995 ac Josephson effect in a single quantum channel *Phys. Rev. Lett.* **75** 1831–4
- [14] Cuevas J C, Hammer J, Kopu J, Viljas J K and Eschrig M 2006 Proximity effect and multiple Andreev reflections in diffusive superconductor-normal-metal-superconductor junctions *Phys. Rev. B* **73** 184505
- [15] Kjaergaard M, Suominen H J, Nowak M P, Akhmerov A R, Shabani J, Palmstrøm C J, Nichele F and Marcus C M 2017 Transparent semiconductor-superconductor interface and induced gap in an epitaxial heterostructure Josephson junction *Phys. Rev. Appl.* **7** 034029
- [16] San-Jose P, Cayao J, Prada E and Aguado R 2013 Multiple Andreev reflection and critical current in topological superconducting nanowire junctions *New J. Phys.* **15** 075019
- [17] Aminov B A, Golubov A A and Kupriyanov M Y 1996 Quasiparticle current in ballistic constrictions with finite transparencies of interfaces *Phys. Rev. B* **53** 365–73
- [18] Rosenbach D *et al* 2020 Quantum transport in topological surface states of selectively grown Bi_2Te_3 nanoribbons *Adv. Electron. Mater.* **6** 2000205
- [19] Weyrich C *et al* 2016 Growth, characterization, and transport properties of ternary $(\text{Bi}_{1-x}\text{Sb}_x)_2\text{Te}_3$ topological insulator layers *J. Phys.: Condens. Matter* **28** 495501
- [20] Plucinski L, Mussler G, Krumrain J, Herdt A, Suga S, Grützmacher D and Schneider C M 2011 Robust surface electronic properties of topological insulators: Bi_2Te_3 films grown by molecular beam epitaxy *Appl. Phys. Lett.* **98** 222503
- [21] QDevil ApS The QFilter - A compact high-performance low-pass filter (available at: <https://qdevil.com/qfilter/>)
- [22] Courtois H, Meschke M, Pelttonen J T and Pekola J P 2008 Origin of hysteresis in a proximity Josephson junction *Phys. Rev. Lett.* **101** 067002
- [23] Blonder G E, Tinkham M and Klapwijk T M 1982 Transition from metallic to tunneling regimes in superconducting microconstrictions: excess current, charge imbalance, and supercurrent conversion *Phys. Rev. B* **25** 4515–32
- [24] Artemenko S N, Volkov A F and Zaitsev A V 1979 On the excess current in microbridges S–c–S and S–c–N *Solid State Commun.* **30** 771–3
- [25] Bardas A and Averin D V 1997 Electron transport in mesoscopic disordered superconductor-normal-metal-superconductor junctions *Phys. Rev. B* **56** R8518–R21
- [26] Volkov A F, Zaitsev A V and Klapwijk T M 1993 Proximity effect under nonequilibrium conditions in double-barrier superconducting junctions *Physica C* **210** 21–34
- [27] Using the BCS interpolation formula $\Delta(T) = 1.76k_B T_c \tanh(1.74\sqrt{T_c/T - 1})$
- [28] Kampmeier J, Weyrich C, Lanius M, Schall M, Neumann E, Mussler G, Schäpers T and Grützmacher D 2016 Selective area growth of Bi_2Te_3 and Sb_2Te_3 topological insulator thin films *J. Cryst. Growth* **443** 38–42
- [29] Ngabonziza P, Wang Y and Brinkman A 2018 Bulk contribution to magnetotransport properties of low-defect-density Bi_2Te_3 topological insulator thin films *Phys. Rev. Mater.* **2** 044204
- [30] Hikami S, Larkin A I and Nagaoka Y 1980 Spin-orbit interaction and magnetoresistance in the two dimensional random system *Prog. Theor. Phys.* **63** 707–10
- [31] Mannila E T, Samuelsson P, Simbierowicz S, Pelttonen J T, Vesterinen V, Grönberg L, Hassel J, Maisi V F and Pekola J P 2022 A superconductor free of quasiparticles for seconds *Nat. Phys.* **18** 145–8
- [32] Schmitt T W *et al* 2022 Integration of topological insulator Josephson junctions in superconducting qubit circuits *Nano Lett.* **22** 2595–602
- [33] Hyart T, van Heck B, Fulga I C, Burrello M, Akhmerov A R and Beenakker C W J 2013 Flux-controlled quantum computation with Majorana fermions *Phys. Rev. B* **88** 035121
- [34] Schüffelgen P *et al* 2017 Stencil lithography of superconducting contacts on MBE-grown topological insulator thin films *J. Cryst. Growth* **477** 183–7
- [35] Charpentier S *et al* 2017 Induced unconventional superconductivity on the surface states of Bi_2Te_3 topological insulator *Nat. Commun.* **8** 2019
- [36] Delacour C, Ortega L, Faucher M, Crozes T, Fournier T, Pannetier B and Bouchiat V 2011 Persistence of superconductivity in niobium ultrathin films grown on R-plane sapphire *Phys. Rev. B* **83** 144504
- [37] Nguyen C, Kroemer H and Hu E L 1992 Anomalous Andreev conductance in InAs-AlSb quantum well structures with Nb electrodes *Phys. Rev. Lett.* **69** 2847–50
- [38] Tomi M, Samatov M R, Vasenko A S, Laitinen A, Hakonen P and Golubev D S 2021 Joule heating effects in high-transparency Josephson junctions *Phys. Rev. B* **104** 134513
- [39] Galaktionov A V and Zaikin A D 2002 Quantum interference and supercurrent in multiple-barrier proximity structures *Phys. Rev. B* **65** 184507
- [40] Usadel K D 1970 Generalized diffusion equation for superconducting alloys *Phys. Rev. Lett.* **25** 507–9
- [41] Kurpianov M Y and Lukichev V F 1988 Influence of boundary transparency on the critical current of dirty SS'S structures *Sov. Phys.-JETP* **67** 1163–8
- [42] Forschungszentrum Jülich GmbH 2017 HNF—Helmholtz nano facility, journal of large scale research facilities **3** A112